Optimizing SWIPT in Multi-RIS aided V2I Networks: A Deep Learning Approach

Manojkumar B. Kokare*, Sumit Gautam*, Swaminathan R.*, Neha Sharma*, Aryan Kaushik †, and Symeon Chatzinotas‡
*Department of Electrical Engineering, Indian Institute of Technology Indore, India
†Department of Computing and Mathematics, Manchester Met, United Kingdom
‡Interdisciplinary Centre for Security, Reliability and Trust (SnT), University of Luxembourg, Luxembourg
Email:{phd2201102016, sumit.gautam, swamiramabadran, phd2201102021}@iiti.ac.in, a.kaushik@ieee.org, symeon.chatzinotas@uni.lu

***Abstract*—This paper investigates the effectiveness of employing multiple reconfigurable intelligent surfaces (RIS) for simultaneous wireless information and power transfer (SWIPT) in a vehicle-to-infrastructure (V2I) system. The optimal RIS is selected for transmission based on instantaneous signal-to-noise ratio (SNR) values, with the objective of optimizing the SWIPT system employing the power-splitting (PS) protocol and non-linear energy harvesting (NL-EH). A unified objective is proposed to maximize information rate and harvested energy via joint optimization of transmit power and power splitting factor. Non-convexity is addressed via an iterative algorithm, supported by closed-form expressions obtained through Karush-Kuhn-Tucker (KKT) conditions. Monte-Carlo simulations are performed to validate the accuracy of the analytical expressions. Additionally, a deep neural network (DNN) framework is introduced for real-time optimization prediction, achieving superior SWIPT performance over single RIS configurations with reduced complexity and faster execution.**

***Index Terms*—Deep neural network (DNN), multi-RIS, simultaneous wireless information and power transfer (SWIPT), reconfigurable intelligent surfaces (RIS), and vehicle-to-infrastructure (V2I).**

I. Introduction

Simultaneous wireless information and power transfer (SWIPT) has emerged as a pioneering concept aimed to meet the escalating demand for sustainable high data-rate services. SWIPT technology enables wireless devices not only to receive data but also to harvest energy from the received signals concurrently [1]. SWIPT operates via two primary protocols: time-switching (TS) and power-splitting (PS). TS divides the channel coherence interval into distinct time slots, enabling simultaneous information decoding and energy harvesting (EH). Conversely, PS partitions the received signal power for distinct operations, facilitating efficient utilization of the available energy resources [2].

To address the inherent challenges faced by SWIPT systems, particularly in adverse radio propagation environments, recent research proposes an integration of reconfigurable intelligent surfaces (RISs) with SWIPT systems [3]. RISs are composed of electromagnetic meta-materials and exhibit the ability to manipulate electromagnetic waves by introducing controlled delays and phase shifts [4]. This enhances the signal-to-noise ratio (SNR) at the receiver, which facilitates more effective utilization of SWIPT.

In [5], the authors presented a novel framework utilizing RISs to enhance SWIPT in non-orthogonal multiple access (NOMA) networks for the ultramassive machine type communications (umMTC) scenario, aiming to maximize the uplink sum rate of the IoT devices by optimizing the TS coefficient, the transmit power of the base station, the RIS phase shifts, and the power allocation coefficients, by alternating optimization (AO) algorithm. The RIS-aided SWIPT system performance was investigated in [3], deriving bounds for rate and energy with TS and PS protocols considering both linear and non-linear (NL) EH models.

In [6], the authors investigated a SWIPT-enabled RIS-assisted multiple-input-multiple-output (MIMO) communication network. A power minimization problem was formulated, which jointly optimizes the active beamforming matrix at the base station (BS) and passive beamforming matrix at the RIS. Authors in [7] studied resource allocation for a multiuser RIS-aided SWIPT system, highlighting the trade-off between maximizing data sum-rate and total harvested energy by jointly optimizing beamforming at the BS and phase shifts at the RIS using a multiobjective optimization framework. In [8], the system's energy efficiency was maximized by jointly designing transmit beamforming at the BS, phase shifts at the RIS, and the PS ratio at users, while adhering to minimum rate, minimum harvested energy, and transmit power constraints. Authors in [9] investigated the outage and symbol error rate performance analysis of a multi-RIS assisted vehicle-to-vehicle (V2V) system over a generalized fading channel. In [10], the authors examined a multi-RIS assisted vehicle-to-infrastructure (V2I) system with SWIPT integration. However, their work does not consider an incorporation of a deep neural network (DNN) architecture. Authors in [11] formulated the computation offloading policy using deep reinforcement learning in a vehicle-assisted vehicular edge computing network. Previous research has mainly concentrated on single RIS-assisted SWIPT for V2I communication, creating a gap in the exploration of SWIPT with multiple RISs over generalized fading channels, as well as the implementation of a DNN model.

From exisiting works in the literature, it is evident that

only a few have addressed multi-RIS assisted V2I systems which incorporate SWIPT, small-scale path loss, the double generalized gamma (dGG) fading channel model, along with a DNN architecture. Therefore, a comprehensive analysis is crucial for the practical implementation of such systems. In this regard, this paper introduces a multi-RIS assisted V2I SWIPT system, alongside a DNN architecture designed to predict the optimal values. The key contributions of this paper are as follows

1) This paper explores enhancing V2I communication via integration of multiple RISs, using a dGG fading channel model, and introduces a strategic RIS selection method based on instantaneous SNR to achieve improved signal quality.
2) A unified optimization problem is formulated to maximize the rate and harvested energy and it is solved using an iterative algorithm along with a closed-form solution derived using Karush-Kuhn-Tucker (KKT) conditions. In addition, a DNN architecture is also proposed to predict the optimal values for rate and harvested energy.
3) The proposed analytical expressions have been thoroughly validated using extensive Monte-Carlo simulations. The results show a marked improvement in system performance and a notable reduction in execution time, highlighting the effectiveness of DNN-based multi-RIS enabled SWIPT systems for future wireless networks.

II. System and Channel Models

We consider a multi-RIS aided V2I SWIPT system, as shown in Fig. 1. Here, a single-antenna source (S) vehicle simultaneously transmits both information and power to the destination (D) vehicle through L multiple RISs, each $\{RIS_l\}_{l=1,\ldots,L}$ consisting of M elements. The setup assumes that direct communication between S and D is not feasible, thus requiring the RISs as the exclusive transmission medium. Furthermore, SWIPT is employed at D using the PS protocol. We consider $\tilde{g}_{l,m} = \left|g_{l,m}\right| e^{j\xi_{l,m}}$ and $\tilde{h}_{l,m} = \left|h_{l,m}\right| e^{j\vartheta_{l,m}}$ as the channel fading coefficients between S and m^{th} element of RIS_l and between the m^{th} element of RIS_l and D respectively, with phases $\xi_{l,m}, \vartheta_{l,m} \in [0, 2\pi]$. The fading channel coefficients $\left|g_{l,m}\right|$ and $\left|h_{l,m}\right|$ follow an independent and non-identically distributed dGG distribution with shaping parameters $(\alpha^{(1)}_{l,m}, \beta^{(1)}_{l,m}, \alpha^{(2)}_{l,m}, \beta^{(2)}_{l,m})$ and $(\alpha^{(3)}_{l,m}, \beta^{(3)}_{l,m}, \alpha^{(4)}_{l,m}, \beta^{(4)}_{l,m})$, respectively [9]. The dGG distribution is considered in a V2I scenario due to its versatility in accurately modeling different distributions like double-Rayleigh and gamma-gamma as its special case. Further, we consider a low speed vehicular (LSV) mobility model, where vehicles remain static during consecutive time slots of transmission [12][1].

The signal received at D, assisted by RIS_l, is expressed as

$$y = \sqrt{P_t} A_l \left(\sum_{m=1}^{M} \tilde{g}_{l,m} \tilde{h}_{l,m} e^{j\phi_{l,m}} \right) x + n_D, \tag{1}$$

[1]This is a realistic assumption, as vehicles typically drive slowly at road intersections, junctions, etc., or parked at a place.

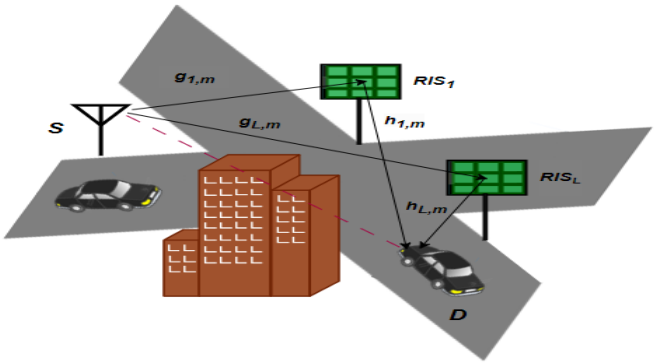

Figure 1: A road intersection scenario where vehicles in blocked line-of-sight can communicate via multi-RIS.

where P_t represents the transmit power of the signal, $e^{j\phi_{l,m}}$ is the phase shift of the m^{th} reflecting element of the RIS_l $\phi_{l,m} \in [0, 2\pi)$, x is the transmit signal/symbol, n_D denotes the additive white Gaussian noise (AWGN) with $n_D \sim \mathcal{CN}(0, N_0)$, and A_l represents free-space path-loss given by [9]

$$A_l = \frac{\lambda^2 \sqrt{G_1 G_2}}{16\pi d_{1,l} d_{2,l}}, \tag{2}$$

where λ denotes the wavelength, G_1 and G_2 are the transmit and receive antenna gains, respectively, and $d_{1,l}$ and $d_{2,l}$ represent distance from S to RIS_l and RIS_l to D, respectively.

The received instantaneous SNR associated with RIS_l at D is expressed as

$$\gamma_l = \frac{P_t A_l^2 \left| \sum_{m=1}^{M} g_{l,m} h_{l,m} e^{j(\xi_{l,m} + \vartheta_{l,m} + \phi_{l,m})} \right|^2}{N_0} = \frac{P_t z_l^2}{N_0}, \tag{3}$$

where $z_l^2 = A_l^2 \left| \sum_{i=1}^{M} g_{l,m} h_{l,m} \right|^2$ and the phase shift of m^{th} element in RIS_l is adjusted such that the total phase shift $\xi_{l,m} + \vartheta_{l,m} + \phi_{l,m} = 0$.

A. Optimal RIS selection

It is to be noted that adopting a strategy to select the optimal RIS can lead to a more energy-efficient multi-RIS aided system. The RIS with the highest end-to-end instantaneous SNR among the available RISs will be considered at D for further processing and the signals coming from other RISs will be discarded [9], [13][2]. Consequently, the end-to-end instantaneous SNR of the selected RIS can be expressed as

$$\hat{\gamma}_{max} = \max_{l=1,\ldots,L} \{\gamma_l\}. \tag{4}$$

The channel state information (CSI) is estimated at D using pilot symbols before each transmission phase and the corresponding instantaneous SNR of each RIS is calculated at the D to perform the best RIS selection.

[2]Discarding signals from non-selected RISs offer low signal processing complexity, as only N received signals need to be processed instead of the $L * N$ signals from all participating RISs.

B. Energy harvesting model and SWIPT protocol

The energy gathered in real-life scenarios is a NL function of the input radio frequency (RF) signal. Normally, when input power increases, the efficiency of converting radio frequency (RF) energy to direct current (RF-to-DC) energy rises to a peak and then levels out at a constant amount. In a high power regime, the harvesting of energy could be overestimated, when the traditional linear EH model is applied. In order to eliminate the inaccuracy of the conventional linear EH receiver model and capture the NL characteristic of the RF-to-DC power conversion, we adopt a sigmoidal function based NL-EH mechanism [14].

We take into consideration the PS scheme for SWIPT, which involves block transmission over T seconds. In the PS scheme, the signal received at D is split into two parts: a fraction $\sqrt{\beta}y$ is provided to EH at D and the remaining $\sqrt{1-\beta}y$ signal decodes the information. The PS-SWIPT receiver yields an expression for the harvested energy as

$$E_h = \frac{T\varepsilon}{1-\Phi}\left(\frac{1}{1+exp(-\beta a P_t z_{max}^2 + ab)} - \Phi\right), \tag{5}$$

where $\Phi = \frac{1}{1+exp(ab)}$ is a constant for the zero-input/zero-output response of EH, z_{max} is channel corresponding to $\hat{\gamma}_{max}$, a and b are the constants related to circuit specifications, β is the PS factor, and ε is the EH circuit saturation point. Correspondingly, the overall rate at the D is given by

$$R = \log_2(1 + (1-\beta)\hat{\gamma}_{max}). \tag{6}$$

The formulation of the optimization problem and the proposed solutions are discussed in the subsequent section.

III. Problem Formulation and Proposed Solution

This section provides the unified problem formulation for optimizing two separate objectives: rate and harvested energy. The optimal values of β and P_t are sought while ensuring rate, harvested energy, P_t, and β stay within defined limit. The metric we define is $\psi_j\{P_t,\beta\}$. It takes the following two different cases: rate $\psi_u\{P_t,\beta\}$ and harvested energy $\psi_v\{P_t,\beta\}$. These cases are expressed as follows

$$\underset{\forall j\in[u,v]}{\psi_j\{P_t,\beta\}} := \begin{cases} \psi_u\{P_t,\beta\} = R & : \text{Rate} \\ \psi_v\{P_t,\beta\} = E_h & : \text{EH} \end{cases} \tag{7}$$

The objective of problem (P1) is to maximize the metric $\psi_j\{P_t,\beta\}$, where j corresponds to maximizing either the rate $\psi_u\{P_t,\beta\}$ or harvested energy $\psi_v\{P_t,\beta\}$. The unified optimization problem is mathematically defined as

$$\begin{aligned} (P1): \underset{P_t,\,\beta}{\text{maximize}} \quad & \psi_j\{P_t,\beta\} \quad \forall j \in [u,v] \\ \text{subject to:} \quad & (C1):\ 0 \le P_t \le P_{max}, \\ & (C2):\ 0 \le \beta \le 1, \\ & (C3):\ R \ge R_{th}, \\ & (C4):\ E_h \ge E_{th}, \end{aligned} \tag{8}$$

Algorithm 1 Iterative AO Algorithm.

1: Initialize $\psi_j\{P_t,\beta\} \quad \forall j \in [u,v]$
2: **Repeat**
3: Solve $(P1)$ for fixed β to obtain P_t^*
4: Solve $(P1)$ by putting P_t^* obtained in 3:, to find β^*
5: Find $\psi_j\{P_t,\beta\}$ using P_t^* and β^*, save $\psi_j\{P_t,\beta\}(n)$ and $n = n+1$
6: **Until**: $\psi_j\{P_t,\beta\}(n) \ge \psi_j\{P_t,\beta\}(n-1)$

where P_{max}, R_{th}, and E_{th} are the maximum transmit power, rate threshold, and harvested energy threshold, respectively.

To address the non-convexity of $(P1)$, we adopt an iterative optimization approach inspired by AO and proposed Algorithm 1. In Algorithm 1, we initialize $\psi_j\{P_t,\beta\} \quad \forall j \in [u,v]$. Firstly, we fix β and compute P_t^*. Secondly, we find β^* by using obtained P_t^* values from step 3. Then the optimized β^* and P_t^* values are used to solve $\psi_j\{P_t,\beta\}$. If the current value of $\psi_j\{P_t,\beta\}$ is less than the past value or if the iterations reach their maximum limit, then we stop the iteration. Otherwise, we save the values and the iterations keep going until a lower value is encountered. With n iterations, its computational complexity is $\mathcal{O}(n\mathcal{ST})$, where $\mathcal{S}$ and $\mathcal{T}$ represent computational parameters.

Next, we discuss an alternative method to obtain a closed-form solution for the aforementioned problem $(P1)$, wherein we solve it directly using the KKT conditions [15]. To proceed, the Lagrangian corresponding to $(P1)$ is denoted as follows

$$\begin{aligned} \mathcal{L}(P_t,\beta;\lambda_1,\lambda_2,\lambda_3,\lambda_4) = f(P_t,\beta) - \lambda_1 g(P_t,\beta) - \lambda_2 h(P_t,\beta) \\ - \lambda_3 i(P_t,\beta) - \lambda_4 j(P_t,\beta), \end{aligned} \tag{9}$$

where $f(P_t,\beta) = \psi_j\{P_t,\beta\}$, $g(P_t,\beta) = P_t - P_{max}$, $h(P_t,\beta) = \beta - 1$, $i(P_t,\beta) = R_{th} - \log_2(1 + (1-\beta)\hat{\gamma}_{max})$, $j(P_t,\beta) = E_{th} - \frac{T\varepsilon}{1-\Phi}\left(\frac{1}{1+exp(-\beta a P_t z_{max}^2+ab)} - \Phi\right)$ and λ_1, λ_2, λ_3, λ_4 are the Lagrange multipliers for the constraints $(C1)$, $(C2)$, $(C3)$, and $(C4)$, respectively.

For optimal value, $\nabla\mathcal{L}(P_t,\beta;\lambda_1,\lambda_2,\lambda_3,\lambda_4) = 0$ must hold. Thus, we can represent the equations for satisfying the optimality conditions as

$$\begin{aligned} \frac{\partial\mathcal{L}(P_t,\beta;\lambda_1,\lambda_2,\lambda_3,\lambda_4)}{\partial P_t} \Rightarrow \left(\frac{\partial\psi_j\{P_t,\beta\}}{\partial P_t}\right)_{j\in[u,v]} - \lambda_1 \\ + \lambda_3(1-\beta)\mu_1 + \lambda_4\beta\mu_2 = 0, \end{aligned} \tag{10}$$

$$\begin{aligned} \frac{\partial\mathcal{L}(P_t,\beta;\lambda_1,\lambda_2,\lambda_3,\lambda_4)}{\partial \beta} \Rightarrow \left(\frac{\partial\psi_j\{P_t,\beta\}}{\partial \beta}\right)_{j\in[u,v]} - \lambda_2 \\ -\lambda_3 P_t\mu_1 + \lambda_4 P_t\mu_2 = 0, \end{aligned} \tag{11}$$

where $\frac{\partial\psi_u\{P_t,\beta\}}{\partial P_t} = (1-\beta)\mu_1$, $\frac{\partial\psi_v\{P_t,\beta\}}{\partial P_t} = \beta\mu_2$, $\mu_1 = \frac{z_{\max}^2}{\ln 2\cdot N_0(1+\frac{(1-\beta)P_t z_{\max}^2}{N_o})}$, $\mu_2 = \frac{T\varepsilon a Z_{\max}^2 e^{(-aP_t\beta z_{\max}^2+ab)}}{(1-\phi)\left(1+e^{(-\beta aP_t z_{\max}^2+ab)}\right)^2}$, $\frac{\partial\psi_u\{P_t,\beta\}}{\partial\beta} = -P_t\mu_1$ and $\frac{\partial\psi_v\{P_t,\beta\}}{\partial\beta} = P_t\mu_2$.

The conditions for feasibility are given as $g(P_t,\beta), h(P_t,\beta), i(P_t,\beta), j(P_t,\beta) \leq 0$. The complementary slackness expressions are represented as follows

$$\lambda_1 \cdot g(P_t,\beta) = 0; \quad \lambda_2 \cdot h(P_t,\beta) = 0;$$
$$\lambda_3 \cdot i(P_t,\beta) = 0; \quad \lambda_4 \cdot j(P_t,\beta) = 0. \tag{12}$$

The conditions for non-negativity are $\{P_t,\beta,\lambda_1,\lambda_2,\lambda_3,\lambda_4\} \geq 0$, with the additional constraint being $h(P_t,\beta) \geq 0$. If $\lambda_2 \neq 0$, then $h(P_t,\beta) = 0$ implying $\beta = 1$, which is infeasible. Thus, λ_2 must be equal to 0. In the case where the KKT condition holds with $\lambda_3 = 0$ and $\lambda_1, \lambda_4 \neq 0$, we obtain $P_{t_1} = P_{max}$ and $\beta_1 = \frac{b}{P_t z_{\max}^2} - \frac{1}{aP_t z_{\max}^2} \ln\left(\frac{1}{\frac{E_{th}(1-\Phi)}{\varepsilon}+\Phi} - 1\right)$ for $\psi_u\{P_t,\beta\}$. The case where $\lambda_1, \lambda_3, \lambda_4 \neq 0$, we get $\beta_2 = 1 - (2^{R_{th}} - 1)\frac{N_o}{P_t z_{\max}^2}$ and β_1 for $\psi_u\{P_t,\beta\}$, and for $\psi_v\{P_t,\beta\}$, the optimal values are P_{t_1}, β_2, and β_1.

The possible solutions for the unified problem is outlined in below theorem.

Theorem 1. *The optimal values of P_t^* and β^* for $\psi_j\{P_t,\beta\}$ are, respectively, given by*

$$P_t^* := \begin{cases} P_{t_1} & : \quad \psi_u\{P_t,\beta\} \\ P_{t_1} & : \quad \psi_v\{P_t,\beta\}. \end{cases} \tag{13}$$

$$\beta^* := \begin{cases} \min(\beta_1,\beta_2) & : \quad \psi_u\{P_t,\beta\} \\ \max(\beta_1,\beta_2) & : \quad \psi_v\{P_t,\beta\}. \end{cases} \tag{14}$$

Proof. See Appendix A. □

In the following section, we introduce a DNN framework to address the aforementioned challenges.

IV. DNN Based Optimal Solution Prediction

In this section, we present a DNN framework for predicting optimal solutions efficiently, offering reduced computational complexity and faster execution.

A. DNN design, datasets generation, and learning model

Herein, we introduce a DNN design for the prediction of optimal solutions, treating optimal RIS selection criteria as a regression problem in supervised learning for $L = 2$ surfaces. The DNN architecture consists of single input, multiple hidden, and single output layers [16]. The system parameters, which include $P_t \in [1,10]$, $M \in [80,240]$, $\alpha_{1,m}^{(1)} \in [1,3]$, $\beta_{1,m}^{(1)} \in [1,3]$, $d_{1,1} \in [1,5]$, $d_{2,1} \in [1,5]$, $\alpha_{1,m}^{(2)} \in [1,3]$, $\beta_{1,m}^{(2)} \in [1,3]$, $d_{1,2} \in [1,5]$ and $d_{2,2} \in [1,5]$, are given as an input to our DNN model. Optimal values given by KKT conditions for rate and EH optimization are treated as output variables. The resultant dataset $\mathcal{H}$ comprises a row vector containing $h = [F[h], Y_s]$, where each sample h is characterized by feature vector $F[h]$ encompassing all 10 input variables. Each $F[h]$ undergoes simulation, producing distinct output Y_s. To prevent overfitting on the training set and attain accurate results on the test set, Y_s samples are normalized using log normalization for harvested energy dataset. Linear functions are applied to output units, while nonlinear activation functions are used for hidden-level units. We generate 10^5 samples, partitioning them into 80% training and 20% testing sets. The exponential linear unit (eLU) activation function is applied at each hidden layer, offering advantages over ReLU by simplifying optimization, reducing computational complexity, and mitigating vanishing gradient issues. The proposed DNN model consists of 10 input variables, with the input layer and each of the four hidden layers containing 150 neurons, while the output layer consists of a single neuron.

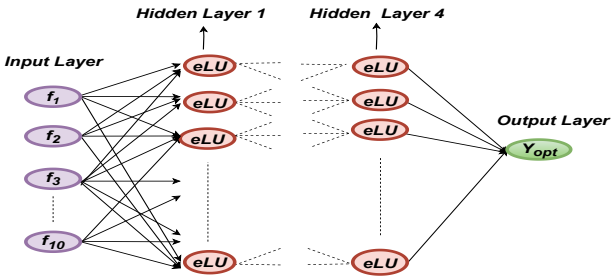

Figure 2: DNN design model.

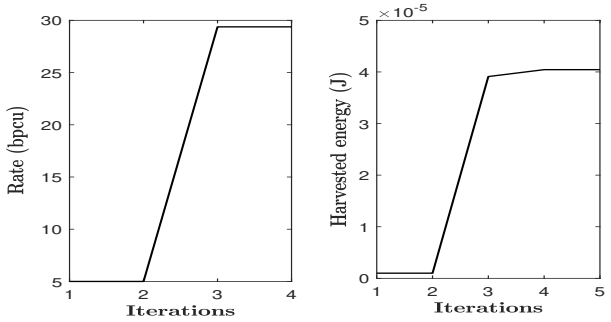

Figure 3: Convergence of rate (bpcu) and harvested energy (J) with iterations.

The DNN framework comprises training and prediction phases. During training, adaptive moment estimation (Adam) optimization is utilized for learning input-output relationships. Adam's efficiency in updating model parameters via back-propagation enhances training speed compared to alternatives such as stochastic gradient descent and Nesterov. Evaluation of model performance on k^{th} testing datasets for predicted output $\widetilde{Y}_{\text{opt}}$ involves computing the mean squared error (MSE) between actual ($Y_s^{(k)}$) and expected ($\widetilde{Y}_{\text{opt}}^{(k)}$) output values as

$$\mathcal{L}(K) = \frac{1}{K}\sum_{k=1}^{K}\left(Y_s^{(k)} - \widetilde{Y}_o^{(k)}\right)^2, \tag{15}$$

where K, $Y_s^{(k)}$, $\widetilde{Y}_o^{(k)}$ are the training samples, the expected value, and the predicted value, respectively. Adam optimization is employed during back-propagation to iteratively update weights and biases, minimizing the training loss. A proficiently trained DNN enables precise real-time predictions. When new input data becomes available, the DNN model predicts corresponding optimal values. During training, DNN configurations can be adjusted to minimize errors and capacity enhancement

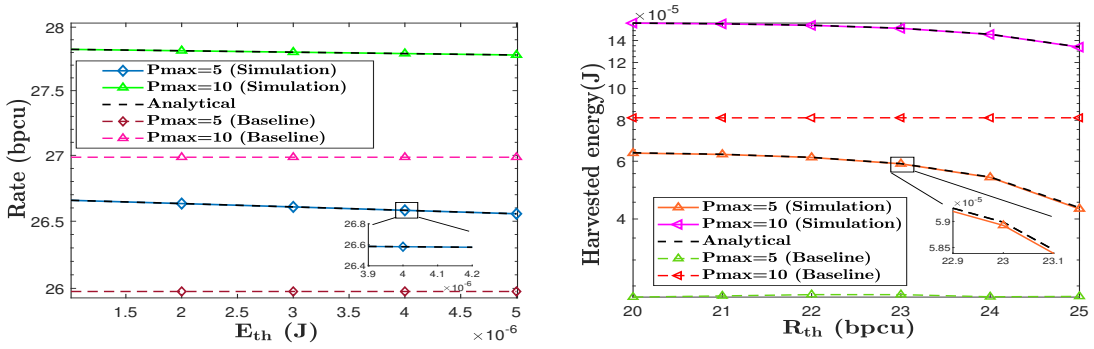

(a) (b)

Figure 4: Rate, and EH: (a) Rate (bpcu) versus E_{th} (J) for different values of maximum P_t and $M = 200$; (b) EH (J) versus R_{th} (bpcu) for different maximum P_t and $M = 200$.

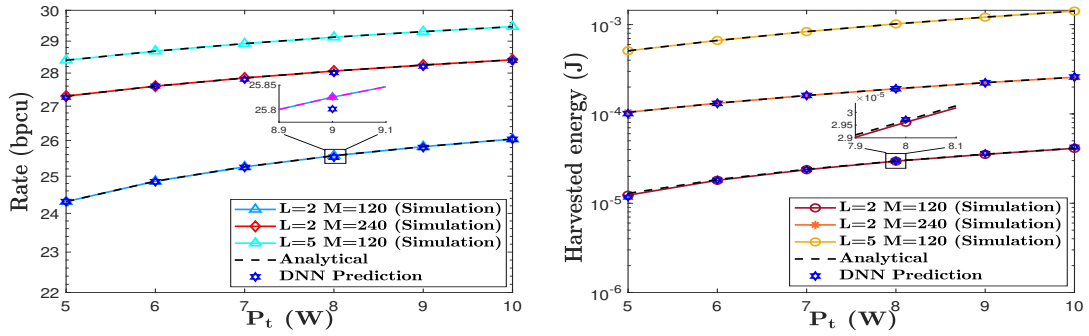

(a) (b)

Figure 5: Rate, and EH: (a) Rate (bpcu) versus P_t (W) for various values of M and L; (b) EH (J) versus P_t (W) for various values of M and L.

by adding more neurons or hidden layers. In the DNN model, computational complexity is mainly determined by the number of floating point operations (FLOPs) and the total number of parameters. For the proposed model, the total number of parameters is 69,601, while the FLOPs are calculated to be 138,901.

V. Numerical Results and Discussions

In this section, we evaluate the numerical results for the considered multi-RIS aided V2I system. The simulation parameters assumed for obtaining the numerical results are given as follows: Transmitter and receiver antenna gains, are chosen as $G_1 = 8$ dBi and $G_2 = 2$ dBi, respectively, $R_{th} = 5$ bpcu, $E_{th} = 1\mu$W, $N_o = -120$ dBW, $\beta = 0.5$, $P_{max} = 10$ W, $\varepsilon = 2.8$ mW, $a = 1500$, and $b = 0.0022$ [17]. We assume identical dGG fading channel parameters for all links for simplicity without loss of generality (i.e. $\alpha_{l,m}^{(1)} = \alpha_{l,m}^{(2)}$ and $\beta_{l,m}^{(1)} = \beta_{l,m}^{(2)}$). Specific dGG fading channel parameters and distances in meters for various RISs are given by $\alpha_{1,m}^{(1)} = 2.5$, $\beta_{1,m}^{(1)} = 2$, $d_{1,1} = 1$, $d_{2,1} = 5$, $\alpha_{2,m}^{(1)} = 2$, $\beta_{2,m}^{(1)} = 2$, $d_{1,2} = 2$, $d_{2,2} = 4$, $\alpha_{3,m}^{(1)} = 1.5$, $\beta_{3,m}^{(1)} = 2$, $d_{1,3} = 3$, $d_{2,3} = 3$, $\alpha_{4,m}^{(1)} = 1$, $\beta_{4,m}^{(1)} = 2$, $d_{1,4} = 4$, $d_{2,4} = 2$, $\alpha_{5,m}^{(1)} = 1$, $\beta_{5,m}^{(1)} = 1$, $d_{1,5} = 5$, $d_{2,5} = 1$. All the results have been evaluated across 500 Monte-Carlo channel realizations.

Fig. 3 illustrates the convergence of both the maximized rate and harvested energy over an average of 500 Monte-Carlo channel realizations, validating the proposed algorithm in Section III. The maximized rate converges in about four iterations, whereas harvested energy convergence takes nearly five iterations.

Fig. 4(a) shows the rate versus E_{th} plot for various P_{max} values. The rate is inversely related to the required EH. The plot indicates that a rate gain of 1 bpcu is attained when P_{max} ranges from 5W to 10W at $E_{th} = 3\mu$J. The analytical solutions, which are derived using KKT conditions, align with the simulations. Fig. 4(b) compares harvested energy versus R_{th} plots for various P_{max} values. The rate-EH trade-off is evident, showing an inverse relationship. The plot indicates that a harvested energy of 15mJ is attained at $P_{max} = 10$W, while 6mJ is achieved at $P_{max} = 5$W, both at $R_{th} = 23$ bpcu. There is a trade-off between data rate and EH based on the PS ratio β. Compared to the baseline with partial optimization of single variable by fixing value of $\beta = 0.5$, increasing the transmit power P_{max} improves both the data rate and harvested energy.

In Fig. 5(a), we examined the rate change with P_t across different M and L values. As expected, higher transmitted power boosts the rate. Moreover, increasing the M and L significantly enhances the rate due to improved instantaneous SNR at D. For $P_t = 9$ W, increasing elements to $M = 120$ results in a 2 bpcu rate gain, while transitioning from $L = 2$ to $L = 5$ yields

a 4 bpcu rate gain. The analytical solutions obtained via KKT conditions are validated by Monto-Carlo simulations. Notably, it is observed that the predictions from the DNN model closely align with the simulation results. The simulation takes 46.72 seconds, while the DNN predicts the optimized value in 0.2504 seconds. The MSE between simulation and DNN predictions is 0.4252. Fig. 5(b) illustrates the variations in maximized harvested energy varies with P_t for different M values and L RISs. As P_t increases, the SNR for $M = 240$ surpasses that for $M = 120$, boosting harvested energy. More RIS elements and RISs notably enhance harvested energy due to optimal RIS selection. Similar to Fig. 5(a), analytical solutions using KKT conditions are validated by simulations. Further, the DNN's predictions closely match the simulation results, achieving a 98.54% time reduction. While the simulation takes 17.65 seconds, the DNN completes the prediction in 0.2572 seconds with an MSE of 0.0039.

VI. Conclusion

This paper investigated a unified optimization problem in a V2I SWIPT system with multiple RISs to maximize both data rate and EH using the PS protocol under an NL-EH model. We selected the optimal RIS based on the maximum end-to-end instantaneous SNR values between S and D. The optimization problems were solved using iterative AO algorithms, and the closed-form solutions were derived using KKT conditions. Numerical results verified our analysis and provided key insights, showing that the rate-energy trade-off is highly sensitive to the number of reflective elements and RISs. Our analysis also showed that increasing the number of reflecting elements and RISs not only enhances both rate and EH but leads to increased computational time. To address this, we proposed a DNN framework to predict optimized values efficiently with high accuracy and low computational time. Our model currently lacks consideration of mobility and imperfect CSI, which will be explored in the future for a more practical scenario.

VII. Acknowledgement

This research is supported by CRG (CRG/2021/0008813) and MATRICS schemes (MTR/2021/000553) of SERB, Govt. of India.

Appendix A
Evaluation of Various Cases From KKT Conditions for Unified Problem

Analyzing (9)-(12) using standard KKT procedures gives below feasible solutions.

Case I: $\lambda_1, \lambda_3, \lambda_4 = 0$, this case is not possible as $\log_2(1+\gamma) \neq 0$ for both $\psi_u\{P_t,\beta\}$ and $\psi_v\{P_t,\beta\}$.

Case II: $\lambda_1, \lambda_3 = 0, \lambda_4 \neq 0$, from (10) $\Rightarrow \lambda_4 < 0$, which is contradictory for both $\psi_u\{P_t,\beta\}$ and $\psi_v\{P_t,\beta\}$.

Case III: $\lambda_1, \lambda_4 = 0, \lambda_3 \neq 0$, from (10) $\Rightarrow \lambda_3 < 0$, which is contradictory for both $\psi_u\{P_t,\beta\}$ and $\psi_v\{P_t,\beta\}$.

Case IV: $\lambda_1 = 0, \lambda_3, \lambda_4 \neq 0$, from (10) and (11)$\Rightarrow \lambda_4 < 0$, its contradictory for both $\psi_u\{P_t,\beta\}$ and $\psi_v\{P_t,\beta\}$.

Case V: $\lambda_3, \lambda_4 = 0, \lambda_1 \neq 0$, from (10) and (11) $\Rightarrow \lambda_4 < 0$, which is contradictory for both $\psi_u\{P_t,\beta\}$ and $\psi_v\{P_t,\beta\}$.

Case VI: $\lambda_3 = 0, \lambda_1, \lambda_4 \neq 0$, then for $\psi_u\{P_t,\beta\}$, from $g(P_t,\beta) = 0 \Rightarrow P_{t_1} = P_{max}$, $j(P_t,\beta_) = 0 \Rightarrow \beta_1 = \frac{b}{P_t z_{max}^2} - \frac{1}{aP_t z_{max}^2} \ln\left(\frac{1}{\frac{E_{th}(1-\Phi)}{\varepsilon}+\Phi} - 1\right)$ and for $\psi_v\{P_t,\beta\}$, from (11) $\Rightarrow \lambda_4 < 0$, which is contradictory.

Case VII: $\lambda_4 = 0, \lambda_1, \lambda_3 \neq 0$, for $\psi_u\{P_t,\beta\}$, from (11) $\Rightarrow \lambda_3 < 0$, which is contradictory and for $\psi_v\{P_t,\beta\}$, from $i(P_t,\beta) = 0 \Rightarrow \beta_2$.

Case VIII: $\lambda_1, \lambda_3, \lambda_4 \neq 0$, for $\psi_u\{P_t,\beta\}$, from $i(P_t,\beta) = 0 \Rightarrow \beta_2 = 1 - (2^{R_{th}} - 1)\frac{N_o}{P_t z_{\max}^2}$ and $j(P_t,\beta) = 0 \Rightarrow \beta_1$ and for $\psi_v\{P_t,\beta\}$, from $g(P_t,\beta) = 0 \Rightarrow P_{t_1}$, $i(P_t,\beta) = 0 \Rightarrow \beta_2$ and $j(P_t,\beta) = 0 \Rightarrow \beta_1$.

Based on the above-mentioned findings, the optimal values of P_t^* and β^* are, respectively, given by (13) and (14).

References

[1] T. D. Ponnimbaduge Perera et al., "Simultaneous wireless information and power transfer (SWIPT): Recent advances and future challenges," *IEEE Commun. Surv. Tutor.*, vol. 20, no. 1, pp. 264–302, 2018.

[2] S. Gautam et al., "Relay selection and resource allocation for SWIPT in multi-user OFDMA systems," *IEEE Wireless Commun. Lett.*, vol. 18, no. 5, pp. 2493–2508, 2019.

[3] D. Gunasinghe and G. A. A. Baduge, "Performance analysis of SWIPT for intelligent reflective surfaces for wireless communication," *IEEE Commun. Lett.*, vol. 25, no. 7, pp. 2201–2205, 2021.

[4] E. Basar et al., "Wireless communications through reconfigurable intelligent surfaces," *IEEE Access*, vol. 7, pp. 116 753–116 773, Aug. 2019.

[5] M. B. Goktas et al., "IRS and SWIPT-assisted full-duplex NOMA for 6G umMTC," *IEEE trans. green commun. netw.*, vol. 7, no. 4, pp. 1957–1970, 2023.

[6] J. Yaswanth et al., "Energy-efficient beamforming design for RIS-aided MIMO downlink communication with SWIPT," *IEEE trans. green commun. netw.*, vol. 7, no. 3, pp. 1164–1180, 2023.

[7] A. Khalili et al., "Multi-objective resource allocation for IRS-aided SWIPT," *IEEE Wireless Commun. Lett.*, vol. 10, no. 6, pp. 1324–1328, 2021.

[8] S. Zargari et al., "Max-min fair energy-efficient beamforming design for intelligent reflecting surface-aided SWIPT systems with non-linear energy harvesting model," *IEEE Trans. Veh. Technol.*, vol. 70, no. 6, pp. 5848–5864, 2021.

[9] M. B. Kokare, R. Swaminathan, and S. Gautam, "Performance of multiple IRS-enabled V2V communication over double generalized gamma fading channel," in *proc. 2024 IEEE COMSNETS*, 2024, pp. 913–919.

[10] M. B. Kokare, S. Gautam, and R. Swaminathan, "On efficient resource allocation strategies for multi-RIS enhanced V2I SWIPT systems," in *proc. 2024 IEEE WCNC*, 2024, pp. 1–6.

[11] L. Geng, H. Zhao, J. Wang, A. Kaushik, S. Yuan, and W. Feng, "Deep-reinforcement-learning-based distributed computation offloading in vehicular edge computing networks," *IEEE Internet Things J.*, vol. 10, no. 14, pp. 12 416–12 433, 2023.

[12] G. Singh et al., "Visible light and reconfigurable intelligent surfaces for beyond 5G V2X communication networks at road intersections," *IEEE Trans. Veh. Technol.*, vol. 71, no. 8, pp. 8137–8151, 2022.

[13] M. Aldababsa et al., "Multiple RISs-aided networks: Performance analysis and optimization," *IEEE Trans. Veh. Technol.*, vol. 72, no. 6, pp. 7545–7559, Jun. 2023.

[14] E. Boshkovska et al., "Practical non-linear energy harvesting model and resource allocation for SWIPT systems," *IEEE Commun. Lett.*, vol. 19, no. 12, pp. 2082–2085, 2015.

[15] S. Boyd and L. Vandenberghe, *Convex optimization*. Cambridge university press, 2004.

[16] C. D. Ho et al., "Short-packet communications in wireless-powered cognitive IoT networks: Performance analysis and deep learning evaluation," *IEEE Trans. Veh. Technol.*, vol. 70, no. 3, pp. 2894–2899, Mar. 2021.

[17] S. Gautam et al., "Experimental evaluation of RF waveform designs for wireless power transfer using software defined radio," *IEEE Access*, vol. 9, pp. 132 609–132 622, 2021.